JOURNAL OF COMPUTATIONAL PHYSICS 115, 228–244 (1994)

A Semi-implicit Ocean Circulation Model Using a Generalized Topography-Following Coordinate System

YUHE SONG AND DALE HAIDVOGEL

Rutgers University, Institute of Marine and Coastal Sciences, P.O. Box 231, New Brunswick, New Jersey 08903

Received July 30, 1993; revised June 7, 1994

We introduce a new ocean circulation model featuring an improved vertical coordinate representation. This new coordinate is a generalized σ-coordinate; however, it is capable of simultaneously maintaining high resolution in the surface layer as well as dealing with steep and/or tall topography. The model equations are the three-dimensional, free surface, primitive equations with orthogonal curvilinear coordinates in the horizontal and the new general coordinate in the vertical. Vertical mixing is treated implicitly by the generalized Crank–Nicolson method based on a Galerkin finite element formulation. Two alternate parameterizations of surface mixing are incorporated, based respectively on the approaches of Price, Weller, and Pinkel and Mellor and Yamada. Finally, a quadrature formula of Lagrange interpolation is employed to produce a more accurate calculation of pressure and vertical velocity. Three tests are used to demonstrate the accuracy, stability, and applicability of the model: the diurnal cycling of the surface mixed layer, flow around a tall seamount, and a regional simulation of the California current system.

1. INTRODUCTION

Successfully meeting the challenge of coupling atmosphere and ocean models greatly depends on the proper representation of surface mixing in the ocean, which in turn requires an appropriate vertical representation of the surface ocean structure where wind and thermal forcing, and vertical turbulent mixing strongly dominate the dynamics. A further, and sometimes competing, requirement is the accurate incorporation of the influences of complex topography and ocean basin geometry. The coastal ocean represents perhaps the most complex modeling challenge, intimately connected as it is to both the deep ocean and the atmosphere, and including strong alongshore and offshore topographic variations. Due to the wide range of conditions present, many frequently employed approximations and simplifications are not applicable [4].

In order to improve the representation of topographic variations, some numerical circulation models use the σ-coordinate system, first introduced by Phillips [22]. The σ-coordinate is a linear function of z which maps the varying topography into a regular domain and greatly simplifies the numerical computations. However, as we show more clearly below, this linear mapping is not consistent with uniformly high resolution at the ocean surface. More recently, vertical stretching [20, 12] and embedding techniques [1] have been used to remedy this problem, but additional difficulties, such as inefficiency and coordinate discontinuity, remain. In this paper, we propose a new general vertical coordinate (hereinafter called an s-coordinate), a nonlinear function of z which allows high resolution in the upper ocean while maintaining the bathymetry—following properties of the σ-coordinate.

It is known that the mapping of an irregular physical domain to a regular computational domain by introducing metric coefficients into the differential operators of the governing equations is advantageous. For some simple geometries, e.g., polar coordinates, these metric coefficients can be calculated analytically. Following Haidvogel *et al.* [12], we employ a nonuniform curvilinear coordinate system which can enhance resolution in specific regions to handle horizontal turbulent mixing and irregular lateral boundaries. A software package is available to generate the orthogonal curvilinear grid system (see Wilkin and Hedström [29]).

In many applications of interest, such as tidal and storm-surge problems [6], the rigid lid assumption is inappropriate. In this model, we explicitly solve the depth-averaged equations for the free surface elevation and depth-averaged velocity field. The depth-averaged equations are discretized on a staggered Arakawa C-grid. A leapfrog prediction–trapezoidal correction scheme is used for the time integration; this is slightly more stable than a leapfrog-only scheme and strongly suppresses the computational mode.

Since wind and thermal forcing and vertical turbulent mixing strongly dominate the surface layer of the ocean, a severe restriction on the size of the allowable time step may result if explicit time-stepping schemes are used. Because of these difficulties, many mixed layer models are based on either one-dimensional or bulk formulations, as reviewed by Henderson-Sellers and Davies [14]. To deal with the strong vertical turbulent mixing, we use the generalized Crank–Nicolson method to treat the vertical mixing dynamics implicitly. This method has been proven stable even for strong vertical advection and diffusion as shown by Lardner and Song [18]. A Galerkin finite element formulation is used to achieve higher accuracy at less cost for a large number of vertical levels.

0021-9991/94 $6.00

Finally, we explore two parameterizations of surface mixing processes: dynamic instability mixing and turbulent closure mixing. Dynamic instability mixing is based on the successful one-dimensional diurnal cycling experiment of Price *et al.* [24]. The model also implements an energy budget form of an entrainment parametrization that is very similar to that described by Price *et al.* [23]. The turbulent closure mixing is based on a level-2 formulation in Mellor and Yamada [21]. The general vertical coordinate system permits a higher resolution in the surface mixed layer, and it enables use of either dynamic stability mixing or energy budget mixing to track the depth of the mixed layer and the transition layer due to surface heating–cooling and wind stirring.

The paper is organized as follows. In Section 2, the primitive equations and accompanying boundary conditions are formulated in the general vertical coordinate system and in the horizontal curvilinear coordinate. In Section 3, the numerical methods used to solve the depth-averaged equations and vertical varying equations are described. Section 4 briefly describes the implementation of the dynamic instability and turbulent closure mixing algorithms. Numerical results are presented in Section 5 for test problems involving diurnal cycling of the surface mixed layer, flow around a tall seamount, and the wind-driven response of the California current system. Conclusions are summarized in Section 6. Finally, Appendix A presents the finite element formulation for the vertical flow structure. Appendix B shows an analytically solvable advection and diffusion problem to test the finite element method. Appendix C describes a quadrature integration technique for the accurate computation of the pressure and vertical velocity.

2. MODEL FORMULATION

2.1. *The Primitive Equations*

We use xyz as Cartesian coordinates with the z-axis pointing vertically upwards and the xy-plane occupying the undisturbed water surface. The horizontal momentum equations can then be written in the form

$$\frac{\partial u}{\partial t} + \mathbf{v}\cdot\nabla u - fv = -\frac{\partial \phi}{\partial x} + \frac{\partial}{\partial z}\left(K_M \frac{\partial u}{\partial z}\right) + \mathfrak{D}_u + \mathfrak{F}_u \quad (2.1)$$

and

$$\frac{\partial v}{\partial t} + \mathbf{v}\cdot\nabla v + fu = -\frac{\partial \phi}{\partial y} + \frac{\partial}{\partial z}\left(K_M \frac{\partial v}{\partial z}\right) + \mathfrak{D}_v + \mathfrak{F}_v. \quad (2.2)$$

The temperature and salinity equations can likewise be written

$$\frac{\partial T}{\partial t} + \mathbf{v}\cdot\nabla T = \frac{\partial}{\partial z}\left(K_H \frac{\partial T}{\partial z}\right) + \mathfrak{D}_T + \mathfrak{F}_T \quad (2.3)$$

and

$$\frac{\partial S}{\partial t} + \mathbf{v}\cdot\nabla S = \frac{\partial}{\partial z}\left(K_H \frac{\partial S}{\partial z}\right) + \mathfrak{D}_S + \mathfrak{F}_S. \quad (2.4)$$

The equation of state and the approximated hydrostatic pressure are

$$\rho = \rho(S, T, P) \quad (2.5)$$

and

$$\frac{\partial \phi}{\partial z} = -\frac{\rho g}{\rho_0}. \quad (2.6)$$

Finally, the continuity equation is

$$\frac{\partial u}{\partial x} + \frac{\partial v}{\partial y} + \frac{\partial w}{\partial z} = 0. \quad (2.7)$$

The equation of state (2.5) can take on different forms for different applications. Generally, it follows the formulation of the international equation of state of sea water [9]. For other cases in which salinity is not explicitly considered, density is a linear function of temperature.

The notation used in these equations is as follows:

u, v, w	the x, y, z components of vector velocity $\mathbf{v}$
$T(x, y, z, t)$	total temperature
$S(x, y, z, t)$	total salinity
$\rho_0 + \rho(x, y, z, t)$	total density
$\phi(x, y, z, t)$	dynamic pressure (P/ρ_0)
P	total pressure
f	Coriolis parameter
g	acceleration due to gravity
$K_M(x, y, z, t)$	vertical eddy viscosity
$K_H(x, y, z, t)$	vertical eddy diffusivity
$\mathfrak{D}_u, \mathfrak{D}_v, \mathfrak{D}_T, \mathfrak{D}_S$	horizontal viscous and diffusive terms
$\mathfrak{F}_u, \mathfrak{F}_v, \mathfrak{F}_T, \mathfrak{F}_S$	forcing terms,

where the vertical eddy coefficients will be discussed further in Section 4. The horizontal viscous and diffusive terms $\mathfrak{D}$ can be the harmonic formulation,

$$\mathfrak{D}_u = A_{MH}\nabla^2 u \equiv A_{MH}\left\{\frac{\partial^2 u}{\partial x^2} + \frac{\partial^2 u}{\partial y^2}\right\}$$

or the biharmonic formulation,

$$\mathfrak{D}_u = -A_{MHB}\nabla^2\nabla^2 u$$

where A_{MH} and A_{MHG} are horizontal viscosity coefficients.

Equations (2.1)–(2.7) are subject to boundary conditions on

the sea surface and at the sea bed. The surface conditions, evaluated at $z = \zeta$, are

$$K_M \frac{\partial u}{\partial z} = \tau_s^x(x, y, t) \tag{2.8}$$

$$K_M \frac{\partial v}{\partial z} = \tau_s^y(x, y, t) \tag{2.9}$$

$$K_H \frac{\partial T}{\partial z} = Q_T/\rho_0 C_p \tag{2.10}$$

$$K_H \frac{\partial S}{\partial z} = (e - p)/\rho_0, \tag{2.11}$$

where τ_s^x and τ_s^y are the components of wind stress acting on the free surface in the x and y directions, respectively; Q_T is the heat fluxes; e and p are the evaporation and precipitation rates, respectively; and C_p is the heat capacity of sea water. Correspondingly, at the sea bed, $z = -h$, the boundary conditions are

$$K_M \frac{\partial u}{\partial z} = \tau_b^x(x, y, t) \tag{2.12}$$

$$K_M \frac{\partial v}{\partial z} = \tau_b^y(x, y, t) \tag{2.13}$$

$$K_H \frac{\partial T}{\partial z} = 0 \tag{2.14}$$

$$K_H \frac{\partial S}{\partial z} = 0, \tag{2.15}$$

where $\tau_b^x = (\gamma_1 + \gamma_2 \sqrt{u^2 + v^2})\, u$ and $\tau_b^y = (\gamma_1 + \gamma_2 \sqrt{u^2 + v^2})\, v$, and γ_1 and γ_2 are coefficients of linear and quadratic bottom friction, respectively.

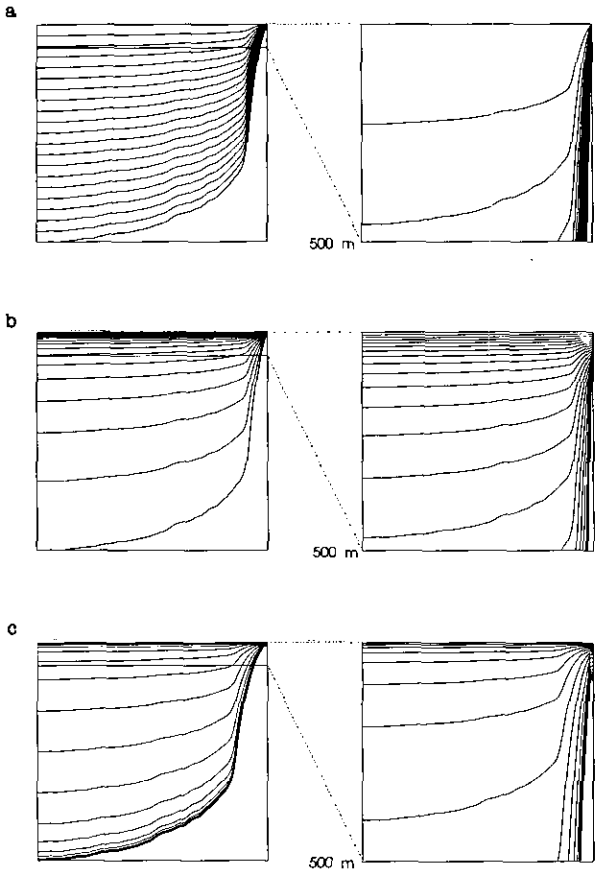

FIG. 1. Vertical computational levels for the California coastal shelf in S-coordinate, left column for the full depth and right column for the upper 500 m: (a) $\theta = 0.0001$, $b = 0$; (b) $\theta = 8$, b = 0; (c) $\theta = 8$, b = 1.

2.2. *General Vertical Coordinate*

The most commonly used vertical coordinate system is the z-coordinate, which naturally represents the physical domain of the ocean as in Eqs. (2.1)–(2.7). In numerical ocean modeling, the grid size in the vertical direction can be easily arranged to allow the highest resolution near the surface and somewhat less resolution below the thermocline. However, great difficulty is encountered in representing varying topography, especially near coastal boundaries where the ocean bottom rapidly varies from shallow to deep water. In such cases, a z-coordinate will approximate the bottom as a series of steps. This may lead to difficulty in applying the bottom kinematic and stress boundary conditions. Another difficulty is the treatment of horizontal mixing of momentum, heat, and salinity; for example, Veronis [28] has pointed out that horizontal mixing in regions of tilted density surfaces can cause a strong spurious upwelling in numerical models.

Another widely used vertical coordinate system is the σ-coordinate. This coordinate transforms the irregular physical domain, bounded by free surface and varying bottom, to a fixed regular computational domain. The advantage of this coordinate is that it follows the bathymetry and greatly simplifies the computation. A corresponding disadvantage is that it cannot maintain equally high resolution near the surface layer independent of local depth. For example, if a coastal region with a minimum inshore depth of 80 m and a maximum offshore depth of 4600 m is represented by a σ-coordinate with 21 equally spaced levels, the grid size is 4 m in shallow water, but 230 m in the offshore region (see Fig. 1a). This kind of resolution is not likely to represent surface mixing processes at all well in the deep ocean.

General vertical coordinate systems have been considered for a long time by meteorologists and oceanographers [20, 16]; however, there is no coordinate system in use which successfully permits uniformly high resolution near the surface like the z-coordinate, yet preserves the bottom following character of the σ-coordinate. In this paper, we will introduce such a general vertical coordinate (s-coordinate) system. Our s-coordinate consists of three terms:

$$z = \zeta(1 + s) + h_c s + (h - h_c)C(s), \quad -1 \le s \le 0, \quad (2.16)$$

where $C(s)$ is a set of s-curves, defined by

$$C(s) = (1 - b)\frac{\sinh(\theta s)}{\sinh \theta} + b\frac{\tanh[\theta(s + 1/2)] - \tanh((1/2)\theta)}{2\tanh((1/2)\theta)},$$

where θ and b are the surface and bottom control parameters. Their ranges are $0 \le \theta \le 20$ and $0 \le b \le 1$, respectively. h_c is a constant chosen to be the minimum depth of the bathymetry or a width of surface or bottom boundary layer in which a higher resolution is required.

The first term in (2.16) is used to follow the free surface $\zeta(x, y, t)$, the second is chosen to prevent possible linear instability, and the third is designed to stretch the interior coordinate lines and to follow the bottom $h(x, y)$. There are three attractive features of this s-coordinate system:

- It is a generalized σ-coordinate system. Letting θ approach zero, by L'Hopital's rule, the s-coordinate becomes the σ-coordinate

$$z = (\zeta + h)(1 + s) - h. \quad (2.17)$$

Numerically, taking $\theta \ll 1$ is sufficient to recover the σ-coordinate system.

- It has a simple linear functional form of $\zeta(x, y, t)$ and $h(x, y)$, and z is an infintely differentiable function of s. Therefore, the formulation of primitive equations in the s-coordinate is similar to that in the σ-coordinate.

- With an equal grid size in s, and by choosing the parameter θ appropriately, the highest resolution is achieved near the surface layer, independently of the varying bottom topography.

Figure 1 shows the s-levels for a vertical section off the California coastal region with a depth of about 80 m at the coast and 4600 m in the interior ocean. Figure 1a is the full depth and the upper 500 m layers of the region for $\theta = 0.0001$ and $b = 0$, corresponding to a traditional σ coordinate. Figure 1b shows the analogous situation for $\theta = 8$ and $b = 0$, maintains high resolution in the surface layer; and Fig. 1c for $\theta = 8$ and $b = 1$, maintains high resolution in the surface and bottom layers. From these plots we can see that, unlike the traditional σ-coordinate system, the s-coordinate can be figured out to maintain its resolution of both surface and bottom layers independent of the local water column depth. It is convenient to define

$$H_\theta \equiv \frac{\partial z}{\partial s} = (\zeta + h_c) + (h - h_c)C_d(s), \quad (2.18)$$

where $C_d(s)$ is the derivative of s-curve $C(s)$, which can be calculated analytically

$$C_d(s) = (1 - b)\frac{\cosh(\theta s)}{\sinh \theta}\theta + b\frac{\coth((1/2)\theta)}{2\cosh^2[\theta(s + 1/2)]}\theta.$$

2.3 *Horizontal Curvilinear Coordinates*

In many applications of interest (e.g., flow adjacent to a coastal boundary), the fluid may be confined horizontally to an irregular region. In such problems, a horizontal curvilinear coordinate system which conforms to the irregular lateral boundaries is advantageous. The most common application of the curvilinear coordinate system in large-scale ocean modeling is the spherical coordinates, where λ, ϕ, and z represent longitude, latitude, and depth, and u, v, and w the zonal, meridional, and vertical components of velocity. In regional or coastal ocean modeling, curvilinear coordinate systems may also be chosen to follow the irregular lateral boundaries and to provide a spatially variable density of coordinate surfaces. A software package developed by Wilkin and Hedström [29] for the generation of such two-dimensional orthogonal grids has been used here. Another advantage to this approach is that it can generate non-uniform curvilinear coordinates with coarser grid spacing over the deep ocean and a finer grid for the shallower coastal region. Because the most severe time-step limitation is related to the local depth of the ocean, this skillful arrangement of the grid can greatly enlarge the time step as shown by Song and Tang [26] in the case of the shallow water equations.

The requirement for a boundary-following coordinate system and for a laterally variable grid resolution can both be met (for suitably smooth domains) by introducing an appropriate orthogonal coordinate transformation in the horizontal. Let the new coordinates be $\xi(x, y)$ and $\eta(x, y)$, where the relationship of horizontal arc length of the differential distance is given by

$$(ds)_\xi = \left(\frac{1}{m}\right)d\xi \quad (2.19)$$

$$(ds)_\eta = \left(\frac{1}{n}\right)d\eta, \quad (2.20)$$

where $m(\xi, \eta)$ and $n(\xi, \eta)$ are the scale factors which relate the differential distances $(\Delta\xi, \Delta\eta)$ to the actual (physical) arc lengths.

Under these horizontal curvilinear coordinate system, the primitive equations (2.1)–(2.7) in the s-coordinate can be written, as shown by Arakawa and Lamb [2] and Kasahara [16],

$$\frac{\partial}{\partial t}\left(\frac{H_\theta u}{mn}\right) + \frac{\partial}{\partial s}\left(\frac{H_\theta \Omega u}{mn}\right) - \frac{\partial}{\partial s}\left(\frac{K_M}{H_\theta mn}\frac{\partial u}{\partial s}\right) - \frac{f}{mn}H_\theta v$$
$$= \left(v\frac{\partial}{\partial \xi}\left(\frac{1}{n}\right) - u\frac{\partial}{\partial \eta}\left(\frac{1}{m}\right)\right)H_\theta v - \frac{H_\theta}{n} \quad (2.21)$$
$$\left\{\frac{\partial \phi}{\partial \xi} + \frac{g\rho}{\rho_0}\left(\frac{\partial z}{\partial \xi}\right)\right\} - \frac{\partial}{\partial \xi}\left(\frac{H_\theta uu}{n}\right) - \frac{\partial}{\partial \eta}\left(\frac{H_\theta uv}{m}\right)$$

$$+\frac{H_\theta}{mn}(\mathfrak{D}_u+\mathfrak{F}_u)$$

$$\frac{\partial}{\partial t}\left(\frac{H_\theta v}{mn}\right)+\frac{\partial}{\partial s}\left(\frac{H_\theta\Omega v}{mn}\right)-\frac{\partial}{\partial s}\left(\frac{K_M}{H_\theta mn}\frac{\partial v}{\partial s}\right)+\frac{f}{mn}H_\theta u$$
$$=-\left(v\frac{\partial}{\partial\xi}\left(\frac{1}{n}\right)-u\frac{\partial}{\partial\eta}\left(\frac{1}{m}\right)\right)H_\theta u-\frac{H_\theta}{m}\left\{\frac{\partial\phi}{\partial\eta}+\frac{g\rho}{\rho_0}\left(\frac{\partial z}{\partial\eta}\right)\right\}-\frac{\partial}{\partial\xi}\left(\frac{H_\theta uv}{n}\right)-\frac{\partial}{\partial\eta}\left(\frac{H_\theta vv}{m}\right)+\frac{H_\theta}{mn}(\mathfrak{D}_v+\mathfrak{F}_v) \tag{2.22}$$

$$\frac{\partial}{\partial t}\left(\frac{H_\theta T}{mn}\right)+\frac{\partial}{\partial s}\left(\frac{H_\theta\Omega T}{mn}\right)-\frac{\partial}{\partial s}\left(\frac{K_H}{H_\theta mn}\frac{\partial T}{\partial s}\right)$$
$$=-\frac{\partial}{\partial\xi}\left(\frac{H_\theta uT}{n}\right)-\frac{\partial}{\partial\eta}\left(\frac{H_\theta vT}{m}\right)+\frac{H_\theta}{mn}(\mathfrak{D}_T+\mathfrak{F}_T) \tag{2.23}$$

$$\frac{\partial}{\partial t}\left(\frac{H_\theta S}{mn}\right)+\frac{\partial}{\partial s}\left(\frac{H_\theta\Omega S}{mn}\right)-\frac{\partial}{\partial s}\left(\frac{K_H}{H_\theta mn}\frac{\partial S}{\partial s}\right)$$
$$=-\frac{\partial}{\partial\xi}\left(\frac{H_\theta uS}{n}\right)-\frac{\partial}{\partial\eta}\left(\frac{H_\theta vS}{m}\right)+\frac{H_\theta}{mn}(\mathfrak{D}_S+\mathfrak{F}_S) \tag{2.24}$$

$$\phi=\frac{g}{\rho_0}\int_s^0 H_\theta\rho(S,T,P)\,ds \tag{2.25}$$

and

$$\frac{\partial}{\partial t}\left(\frac{H_\theta}{mn}\right)+\frac{\partial}{\partial\xi}\left(\frac{H_\theta u}{n}\right)+\frac{\partial}{\partial\eta}\left(\frac{H_\theta v}{m}\right)+\frac{\partial}{\partial s}\left(\frac{H_\theta\Omega}{mn}\right)=0, \tag{2.26}$$

where Ω, $\partial z/\partial\xi$, and $\partial z/\partial\eta$ are defined by

$$\Omega=\frac{1}{H_\theta}\left\{w-(1+s)\frac{\partial\zeta}{\partial t}-um\frac{\partial z}{\partial\xi}-vn\frac{\partial z}{\partial\eta}\right\} \tag{2.27}$$

$$\frac{\partial z}{\partial\xi}=(1+s)\frac{\partial\zeta}{\partial\xi}+C(s)\frac{\partial h}{\partial\xi} \tag{2.28}$$

and

$$\frac{\partial z}{\partial\eta}=(1+s)\frac{\partial\zeta}{\partial\eta}+C(s)\frac{\partial h}{\partial\eta}. \tag{2.29}$$

3. MODEL DISCRETIZATION

3.1 *The External Model Equations*

Equations (2.21)–(2.26) are solved separately for their external mode representing the depth-averaged flow and the internal mode representing vertically varying component. The equations for the vertical variations of momentum, and temperature and salinity will be considered in the next section. The external mode equations can be obtained by vertical integration of the momentum equations (2.21)–(2.22) and the continuity equation (2.26). Using the surface and bottom conditions (2.8)–(2.15), we obtain

$$\frac{\partial}{\partial t}\left(\frac{D\bar u}{mn}\right)=\left\{\frac{f\bar v}{mn}+\overline{vv}\frac{\partial}{\partial\xi}\left(\frac{1}{n}\right)-\overline{uv}\frac{\partial}{\partial\eta}\left(\frac{1}{m}\right)\right\}D-\frac{D}{n}\overline{\left\{\frac{\partial\phi}{\partial\xi}+\frac{g\rho}{\rho_0}\left(\frac{\partial z}{\partial\xi}\right)\right\}}-\left\{\frac{\partial}{\partial\xi}\left(\frac{D\overline{uu}}{n}\right)+\frac{\partial}{\partial\eta}\left(\frac{D\overline{uv}}{m}\right)\right\}+\frac{D}{mn}\overline{(\mathfrak{D}_u+\mathfrak{F}_u)}+\frac{1}{mn}(\tau_s^\xi-\tau_b^\xi) \tag{3.1}$$

$$\frac{\partial}{\partial t}\left(\frac{D\bar v}{mn}\right)=-\left\{\frac{f\bar u}{mn}+\overline{uv}\frac{\partial}{\partial\xi}\left(\frac{1}{n}\right)-\overline{uu}\frac{\partial}{\partial\eta}\left(\frac{1}{m}\right)\right\}D-\frac{D}{m}\overline{\left\{\frac{\partial\phi}{\partial\eta}+\frac{g\rho}{\rho_0}\left(\frac{\partial z}{\partial\eta}\right)\right\}}-\left\{\frac{\partial}{\partial\xi}\left(\frac{D\overline{uv}}{n}\right)+\frac{\partial}{\partial\eta}\left(\frac{D\overline{vv}}{m}\right)\right\}+\frac{D}{mn}\overline{(\mathfrak{D}_v+\mathfrak{F}_v)}+\frac{1}{mn}(\tau_s^\eta-\tau_b^\eta) \tag{3.2}$$

and

$$\frac{\partial}{\partial t}\left(\frac{\zeta}{mn}\right)+\frac{\partial}{\partial\xi}\left(\frac{D\bar u}{n}\right)+\frac{\partial}{\partial\eta}\left(\frac{D\bar v}{m}\right)=0, \tag{3.3}$$

where $D=\zeta+h(x,y)$ and the overbar stands for the depth-averaged integral which for a generic variable A is

$$\bar A=\frac{1}{D}\int_{-1}^0 H_\theta A\,ds.$$

The depth-averaged equations are discretized on a staggered Arakawa C-grid. The semidiscrete form of the equations is

$$\frac{\partial}{\partial t}\left(\frac{D\bar u}{mn}\right)=\left\{\frac{f\overline{\bar v}^{\xi\eta}}{mn}+\overline{(\overline{vv})^\xi}\,\delta_\xi\left(\frac{1}{n}\right)-\overline{(\overline{vv})^\xi}\,\delta_\eta\left(\frac{1}{m}\right)\right\}D-\frac{D}{n}\overline{\left\{\delta_\xi\phi+\frac{g\rho}{\rho_0}(\delta_\xi z)\right\}}-\left\{\delta_\xi\left(\frac{D\overline{uu}}{n}\right)+\delta_\eta\left(\frac{D\overline{uv}}{m}\right)\right\}+\frac{D}{mn}\overline{(\mathfrak{D}_u+\mathfrak{F}_u)}+\frac{1}{mn}(\tau_s^\xi-\tau_b^\xi) \tag{3.4}$$

$$\frac{\partial}{\partial t}\left(\frac{D\bar{v}}{mn}\right) = -\left\{\frac{f\bar{\bar{u}}^{\xi\eta}}{mn} + \overline{(\bar{v}\bar{v})}^{\eta}\,\delta_{\xi}\left(\frac{1}{n}\right) - \overline{(\bar{u}\bar{u})}^{\eta}\,\delta_{\eta}\left(\frac{1}{m}\right)\right\} D$$
$$- \frac{D}{m}\overline{\left\{\delta_{\eta}\phi + \frac{g\rho}{\rho_0}(\delta_{\eta}z)\right\}} - \left\{\delta_{\xi}\left(\frac{D\overline{uv}}{n}\right)\right. \qquad (3.5)$$
$$\left. + \delta_{\eta}\left(\frac{D\overline{vv}}{m}\right)\right\} + \frac{D}{mn}\overline{(\mathfrak{D}_v + \mathfrak{F}_v)}$$
$$+ \frac{1}{mn}(\tau_s^{\eta} - \tau_b^{\eta})$$

and

$$\frac{\partial}{\partial t}\left(\frac{\zeta}{mn}\right) + \delta_{\xi}\left(\frac{D\bar{u}}{n}\right) + \delta_{\eta}\left(\frac{D\bar{v}}{m}\right) = 0, \qquad (3.6)$$

where

$$(\delta_{\xi}A)_{ij} \equiv A_{i+1/2,j} - A_{i-1/2,j}$$
$$(\delta_{\eta}A)_{ij} \equiv A_{i,j+1/2} - A_{i,j-1/2}$$
$$(\bar{A}^{\xi})_{ij} \equiv (A_{i+1/2,j} + A_{i-1/2,j})/2$$
$$(\bar{A}^{\xi\eta})_{ij} \equiv \overline{(\bar{A}^{\xi})}^{\eta}_{ij}.$$

A leapfrog-trapezoidal scheme is used for the time integration; this is slightly more stable than the leapfrog itself and strongly suppresses the computational mode. It should be pointed out that the depth-averaged equations are not independent of the vertically varying equations; they are coupled through the nonlinear and pressure gradient terms. In order to solve the coupled external and internal modes efficiently, a short time step is used for solving the external mode equations in order to satisfy the CFL condition arising from the fast moving gravity waves. An implicit long time step (about 20 times longer than the short one) is used to obtain the internal mode as shown in the next subsection. This splitting technique has been widely used, e.g., by Arakawa and Lamb [2] and Lardner and Smoczynski [17], in many three-dimensional tidal and coastal circulation models.

In Eqs. (3.5)–(3.6), $\overline{uu}$, $\overline{uv}$, and $\overline{vv}$ are evaluated from the internal mode. In the fast time steps, they are replaced by $\overline{uu}$, $\overline{uv}$, and $\overline{vv}$, respectively, and the differences $\overline{uu} - \overline{uu}$, $\overline{uv} - \overline{uv}$, and $\overline{vv} - \overline{vv}$ are only updated at the long time step. The pressure gradient terms are treated similarly.

3.2. *The Internal Mode Equations*

The internal mode equations consist of the momentum equations (2.21)–(2.22) and temperature and salinity equations (2.23)–(2.24). For simplicity, we can write a u-equation and a temperature equation as

$$\frac{\partial H_\theta u}{\partial t} + \frac{\partial(\Omega H_\theta u)}{\partial s} - \frac{\partial}{\partial s}\left(\frac{K_M}{H_\theta}\frac{\partial u}{\partial s}\right) = mnR_u \qquad (3.7)$$

$$\frac{\partial H_\theta T}{\partial t} + \frac{\partial(\Omega H_\theta T)}{\partial s} - \frac{\partial}{\partial s}\left(\frac{K_H}{H_\theta}\frac{\partial T}{\partial s}\right) = mnR_T, \qquad (3.8)$$

where R_u and R_T are

$$R_u = \left\{\frac{f}{mn} + v\frac{\partial}{\partial\xi}\left(\frac{1}{n}\right) - u\frac{\partial}{\partial\eta}\left(\frac{1}{m}\right)\right\} H_\theta v$$
$$- \frac{H_\theta}{n}\left\{\frac{\partial\phi}{\partial\xi} + \frac{g\rho}{\rho_0}\left(\frac{\partial z}{\partial\xi}\right)\right\} - \frac{\partial}{\partial\xi}\left(\frac{H_\theta uu}{n}\right)$$
$$- \frac{\partial}{\partial\eta}\left(\frac{H_\theta uv}{m}\right) + \frac{H_\theta}{mn}(\mathfrak{D}_u + \mathfrak{F}_u)$$
$$R_T = -\frac{\partial}{\partial\xi}\left(\frac{H_\theta uT}{n}\right) - \frac{\partial}{\partial\eta}\left(\frac{H_\theta vT}{m}\right) + \frac{H_\theta}{mn}(\mathfrak{D}_T + \mathfrak{F}_T).$$

The v-equation and salinity equation can be written in the similar forms. The internal mode equations are solved by a semi-implicit hybrid finite element/finite difference method. In detail, the vertical direction is discretized by a Galerkin finite element formulation, which is described in Appendix A. The right-hand-side terms are discretized on the staggered C-grid. The semi-implicit time discretization is shown in the next subsection.

3.3. *Time Discretization*

We shall use the implicit generalized Crank–Nicolson scheme in s and the third-order Adams–Bashforth scheme [7] for the horizontal directions. We use U as the generic variable for Eqs. (3.7)–(3.8) and introduce

$$\tilde{U} = \lambda U^{n+1} + (1 - \lambda)U^n, \qquad (3.9)$$

where λ is an implicitness parameter, and approximate Eq. (3.7) and boundary conditions (2.8)–(2.13) as

$$\frac{H_\theta U^{n+1} - H_\theta U^n}{\Delta t} + \frac{\partial(\Omega H_\theta \tilde{U})}{\partial s} - \frac{\partial}{\partial s}\left(\frac{K}{H_\theta}\frac{\partial\tilde{U}}{\partial s}\right) = mn\tilde{R}_U \qquad (3.10)$$

$$K\frac{\partial\tilde{U}}{\partial s} = H_\theta\tilde{\tau}_s, \quad K\frac{\partial\tilde{U}}{\partial s} = H_\theta\tilde{\tau}_b \qquad (3.11)$$

where $\tilde{\tau}_s$ and $\tilde{\tau}_b$ are the surface and bottom boundary conditions (2.8)–(2.13). K stands for the corresponding vertical eddy coefficient. On the right side, $\tilde{R}_U$ only involves horizontal derivatives and is evaluated explicitly, based on the third-order Adams–Bashforth scheme by

$$\tilde{R}_U = \tfrac{1}{12}(23R^n - 16R^{n-1} + 5R^{n-2}). \qquad (3.12)$$

Treating $\tilde{U}$ as the new unknown, we can rewrite Eq. (3.10) as

$$\frac{H_\theta \tilde{U}}{\lambda \Delta t} + \frac{\partial(\Omega H_\theta \tilde{U})}{\partial s} - \frac{\partial}{\partial s}\left(\frac{K}{H_\theta}\frac{\partial \tilde{U}}{\partial s}\right) = \frac{H_\theta U^n}{\lambda \Delta t} + mn\tilde{R}_U. \quad (3.13)$$

Once $\tilde{U}$ is solved, U^{n+1} can be updated through Eq. (3.9). This treatment of time discretization has several advantages over the traditional leapfrog scheme. The implicit treatment of the vertical direction removes the severe CFL restriction which arises from the very thin vertical grid size near the surface, so that a longer time step can be used. Usually, when the surface turbulent mixing is considered, a higher vertical resolution is necessary to achieve a desired accuracy. In the traditional three-level leapfrog scheme, the diffusion terms have to be treated by an Euler method to avoid unconditional instability, thereby reducing the accuracy to first order. Here, the Adams–Bashforth can achieve third-order accuracy for all right-hand-side terms and reduce the time-splitting oscillation usually associated with the leapfrog scheme.

4. MODEL PARAMETERIZATION

An important and unresolved issue in ocean circulation modeling is the appropriate parameterization of subgridscale processes. One of the purposes of the s-coordinate is to achieve a uniformly high resolution in the surface layer so that mixing parameterizations (whatever they may be) can be accurately applied. Here, we consider two accepted parameterization approaches.

4.1. *Turbulence Closure Mixing*

In this submodel, a Mellor–Yamada level-2 scheme [21] is used to parameterize the vertical eddy viscosity and eddy diffusion coefficients as

$$K_M = lqS_M \quad (4.1)$$

$$K_H = lqS_H, \quad (4.2)$$

where $q^2/2$ is the turbulent kinetic energy, l is the turbulent length scale, and S_M and S_H are functions of Richardson number R_g and satisfy the steady state turbulent kinetic energy (TKE) equation

$$S_M\left[\left(\frac{\partial u}{\partial z}\right)^2 + \left(\frac{\partial v}{\partial z}\right)^2\right] + S_H \frac{g}{\rho}\frac{\partial \rho}{\partial z} = \frac{q^2}{B_1 l^2}. \quad (4.3)$$

In this equation, B_1 is a constant equal to 15 and the length scale l is estimated from the Blackadar boundary layer formation,

$$l = \gamma \int_{z=-h}^{z=\zeta} |z|\, q\, dz \left[\int_{z=-h}^{z=\zeta} q\, dz\right]^{-1},$$

where $\gamma = 0.2$ is a length scale factor. In our model, the TKE equation is solved by a simple diagnostic method of Galperin *et al.* [8].

4.2. *Dynamic Instability Mixing*

Upper ocean density profiles often show a neutrally stable surface layer, or mixed layer which is capped below by a stable stratified layer, the diurnal or seasonal thermocline. The neutrally stable mixed layer is easily stirred by a surface stress or destabilizing surface buoyancy flux, and air–sea exchanges are rapidly distributed through the mixed layer. In this model, we employ the dynamic instability mixing approach to apply the atmospheric forcing and to trap the depth of the mixed layer. This approach is the hybrid mixed layer formulation of Price *et al.* [24] which assumes that the upper ocean density and velocity will be mixed vertically to satisfy the following three stability criteria:

(i) static stability:

$$-\frac{\partial \rho}{\partial z} \geq 0. \quad (4.4)$$

Static instability is generally caused by surface cooling, such a in autumn and winter of the seasonal cycle, and in the evening of the diurnal cycle. This mixing process simulates free convection, which occurs whenever there is heat loss from the sea surface, and is a major process responsible for the deepening of the mixed layer. In our model, the instability is removed by mixing the unstable layer with the layers below as necessary to restore a stably stratified new state.

(ii) mixed layer stability:

$$R_b = \frac{-g\Delta\rho h_m}{\rho_0(\Delta u^2 + \Delta v^2)} \geq 0.65, \quad (4.5)$$

where h_m is the mixed layer depth and Δ takes the difference between the mixed layer and the level just beneath it. R_b is the bulk Richardson number. The second process simulates mixed-layer entrainment and further deepens the mixed layer by relaxation of an overall Richardson number. Price *et al.* [24] show that reducing R_b to a value less than 1 gives significant vertical mixing, which in practice occurs where the mixed layer current is strongly accelerated by the wind stress.

(iii) shear flow stability:

$$R_g = \frac{-g\partial\rho/\partial z}{\rho_0\{(\partial u/\partial z)^2 + (\partial v/\partial z)^2\}} \geq 0.25, \quad (4.6)$$

where R_g is the gradient Richardson number. Rather than deepening the mixed layer like the previous two processes, this mixing process is to stir or smear out the sharp corners within the transition layer. The shear flow stability criterion

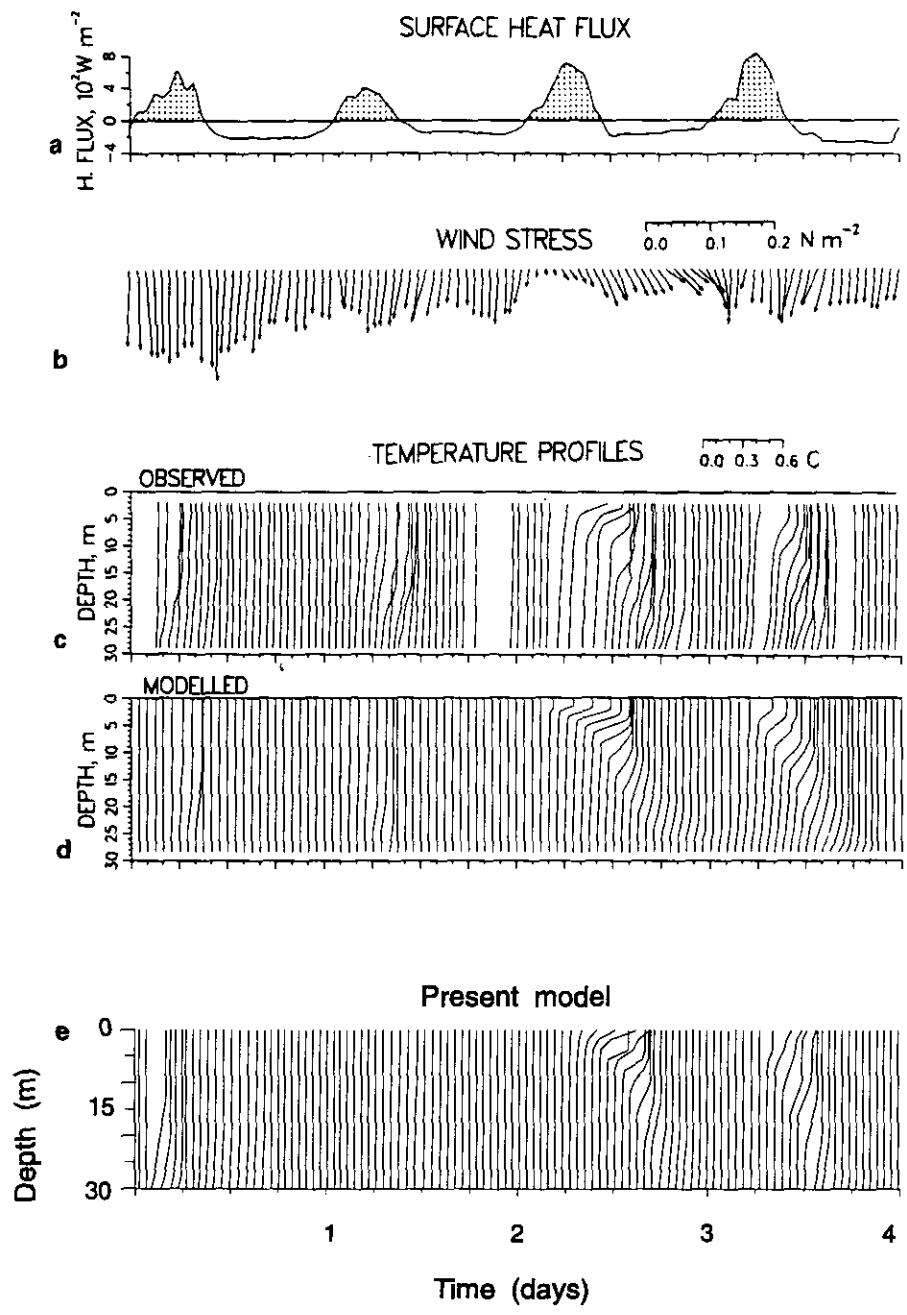

FIG. 2. Time series of (a) surface heat flux, (b) wind stress, (c) observed temperature profiles, (d) computed temperature profiles by Price *et al.*, (e) computed results from the present model.

produces significant mixing in a transition mixed layer when there is significant vertical shear at the base of the mixed layer.

5. MODEL PERFORMANCE

In this section, we choose three widely different problems to demonstrate the capabilities and numerical properties of the model: the diurnal cycling of the surface mixed layer, a tall seamount in a resting ocean, and finally, a simulation of wind-driven California coastal currents.

5.1. *Diurnal Cycle*

A diurnal thermal cycle is well known to occur in the upper ocean whenever the solar heating at midday exceeds the heat loss from the ocean surface. When wind stress effects are considered, more complex surface mixing processes can occur.

TABLE Ia

Values of the Parameters Used in the Diurnal Cycling Problem

Symbol	Value	Definition
N	32	Vertical levels
h_c	100 m	Parameter in s-coordinate
θ	4	Parameter in s-coordinate
H	1000 m	Water depth
$\bar{\rho}$	$4. - 2 \times e^{z/200}$	Background density stratification
K_M	1×10^{-4}	Vertical viscosity coefficient
K_H	0	Vertical diffusivity coefficient

The key to understanding the diurnal cycle is to learn how these changes in the trapping depth depend upon the day-to-day variability in the heating and wind stress.

In this test problem, we use the wind field data and surface heat fluxes from Price *et al.* [24], which are given in a time period of 4 days from day 128 to day 132. The wind field (τ^x, τ^y) and the surface heat flux ($Q_T = I - L$, where I and L are solar insulation and heat loss, respectively) as well as the observed temperature profiles in the first four days are presented in Fig. 2. In order to assess our model by using the one-dimensional results, we also set up the model to a one-dimensional form by eliminating all of the horizontal processes. The total ocean depth is chosen to be 1000 m and upper ocean depth 100 m, with a resolution of 32 levels for total and 24 levels in the upper ocean, respectively. The values of the parameters used in this simulation are shown in Table Ia.

The simulated upper layer temperature profiles are also presented in Fig. 2 for comparison. This result shows a very good agreement with the result of Price *et al.* [24]. We also plotted the full depth of the density profiles in Fig. 3 which shows how the upper layer of the ocean is responding to the diurnal cycling. From these figures we can see that the transition base can reach 60 m below the surface for this 4-day simulation.

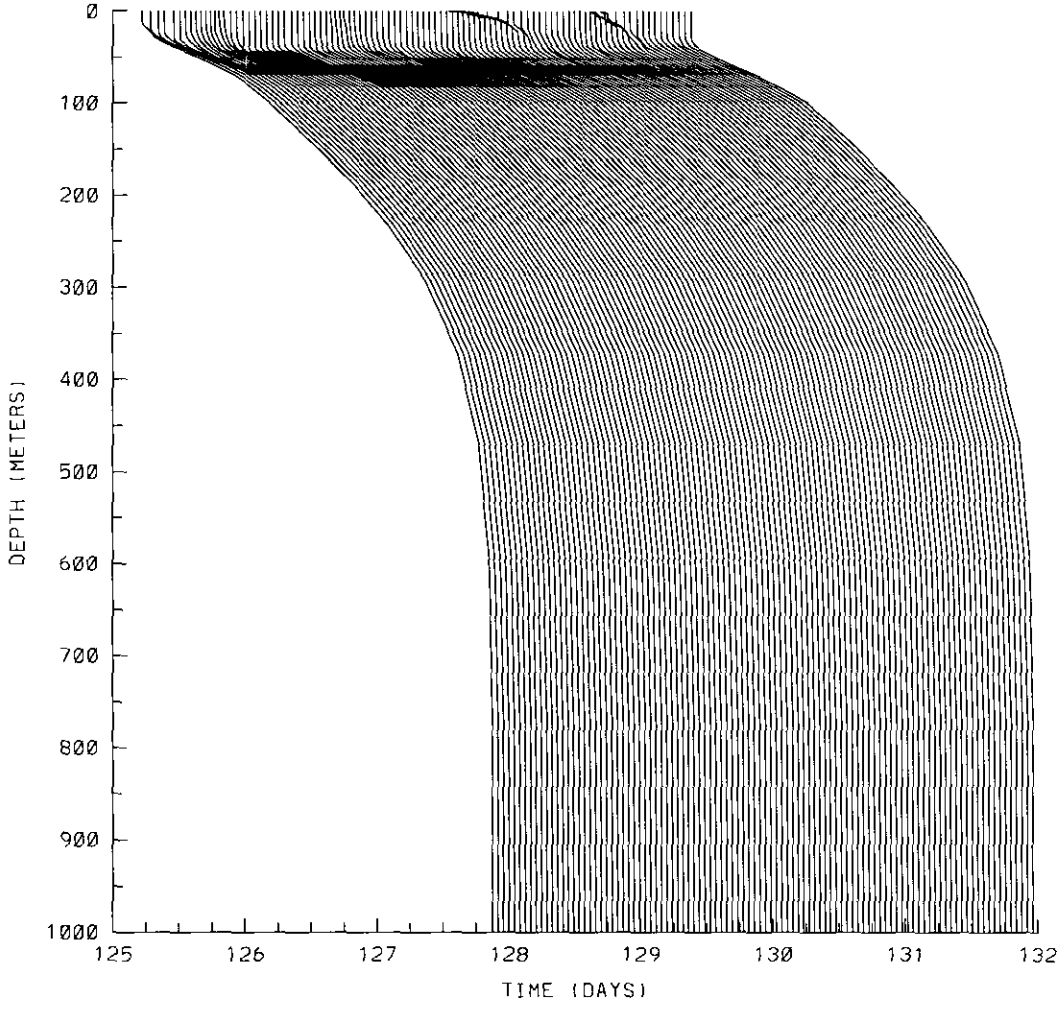

FIG. 3. Time series of whole depth density profiles stirred by the diurnal variability of heating and wind forcing.

TABLE Ib

Values of the Parameters Used in the Seamount Test

Symbol	Value	Definition
L	42	Number of points in ξ direction
M	41	Number of points in η direction
N	30	Vertical levels
h_{min}	500 m	Minimum of water depth
h_{max}	5000 m	Maximum of water depth
$\bar{\rho}$	$4. - 3.8 \times e^{z/1000}$	Background density stratification
A_{M4}	$5 \times 10^3 m^2 s^{-1}$	Harmonic viscosity coefficient
A_{H4}	$1 \times 10^3 m^2 s^{-1}$	Harmonic diffusion coefficient
K_M	$1 \times 10^4 m^2 s^{-1}$	Vertical viscosity coefficient
K_H	$1 \times 10^{-4} m^2 s^{-1}$	Vertical diffusivity coefficient

These properties cannot be simulated without the higher resolution of the surface layer provided by the s-coordinate.

5.2. *A Tall Seamount Topography*

The seamount test case provides a measure of the errors in the pressure gradient term in the presence of steep bathymetry [3, 5]. The configuration is a tall, steep seamount in a channel, closed on the north and south walls and recirculating through the east and west boundaries. The computational domain has dimensions of approximately 320 km by 320 km and is divided into 40 × 40 grid cells. The isolated seamount is located in the center of the channel and its topography can be described by a Gaussian profile,

$$h(x, y) = 5000 - 4500e^{-(r/l)^2},$$

where r is the distance from the center of the domain and D is the width of the seamount. We used $r = 4.5$ km and $l = 40$ km in this test. By virtue of the curvilinear coordinate, finer resolution is achieved near the center of the domain with a 2 : 1 variation in grid spacing from the center to the edges. The enhancement is applied in the same manner in both the x and y directions.

The stratified fluid is represented by a total density profile in the form

$$\rho_{total} = \rho_0 + \bar{\rho}(z) + \{\rho(x, y, z, t) - \bar{\rho}(z)\}$$

$$\bar{\rho}(z) = 4. - \gamma e^{z/1000},$$

where $\rho_0 = 1024$ and $\gamma = 3.8$ kg/m^3 is the density anomaly which corresponds to the Burger number [3]

$$S = \frac{N^2 H^2}{f_0^2 l^2} \approx 11.4,$$

where $N^2 = g\delta_z\rho/\rho_0 H$, and H is the maximum water depth.

The initial conditions for this test are a state of rest, i.e.,

$$u = v = w = 0,$$

and initially level isopycnal surfaces,

$$\rho(z, t = 0) = \bar{\rho}(z).$$

The equation of state is chosen in the form of a single density variable rather than the function of temperature and density. Other parameter values are given in Table Ib.

With these initial conditions and a strongly stratified profile ($\gamma = 3.8$ kg/m^3), we have examined two experiments, one without mixing and another with wind forcing and turbulent mixing. The first experiment consists of two runs, one using the s-coordinate with $\theta = 3$ and another using a σ-coordinate; both cases were run for 10 days. The results from the first run are plotted in Fig. 4 for the sections of zonal velocity u, coordinate levels, vertical velocity w, and initial density ρ through the center of the seamount. The magnitude of the peak velocity after 10 days is 0.83×10^{-3} m/s. Comparable results from the second run, plotted in Fig. 5, shows more numerical noise, especially near the surface layer. The magnitude of the peak velocity in this case is 0.42×10^{-2} m/s, which is about 5 times bigger than that in the first case with the s-coordinate.

In the second experiment, we use the same s-coordinate as in the first experiment, and apply the Mellor–Yamada level-2 turbulent mixing. A constant westward wind ($\tau^x = -1$ dyne/cm^2) is also used to test the surface mixing. Contours of the surface elevation and the surface velocity field driven by the wind are plotted in Fig. 6 and show the expected influence of the seamount [5]. Sections of the velocity components u, v, and w in Fig. 7 clearly show the surface mixed layer generated by the turbulent mixing [14], despite the layer depth variations across the seamount.

From these experiments, we conclude that the model with the general vertical coordinate can handle the combined effects of steep bathymetry and strong stratification as well as prior models based upon the sigma coordinate system.

5.3. *California Coast Region*

The model domain is approximately 1000 km in along-channel length from the south side of Pt. Conception to the north of Cape Blanco, and 700 km in cross-shelf extent. The coastal wall is irregular in shape, featuring a set of capes and bays whose cross-shelf excursions are largest near Cape Mendocina and Pt. Arena. The coastal wall and the offshore boundary are treated as impermeable, free-slip walls. The flow is periodic in the along-channel direction. Using the horizontal orthogonal curvilinear coordinates discussed in Section 2, the computational domain is discretized into 98 by 65 grid cells. The grid cells are nonuniform in size, as shown in Fig. 8.

The underlying bottom topography is smoothed from the realistic data in order to fit the north and south periodic boundary conditions. The minimum and maximum depth values in the

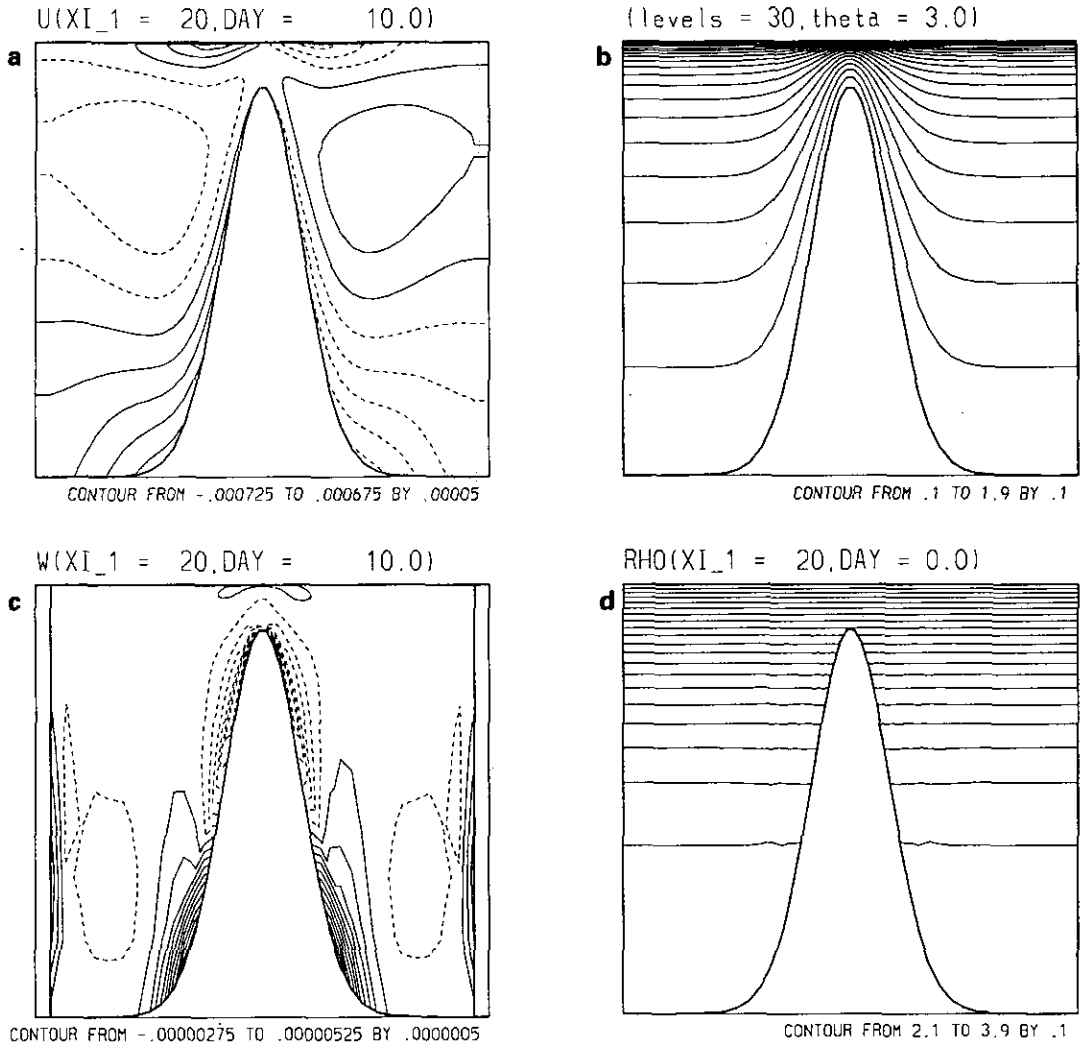

FIG. 4. Contours of cross sections through the center of the seamount: (a) for u; (b) for coordinate levels; (c) for w; and (d) for ρ in s-coordinate.

domain are 86 m at the coastal wall and 4600 m in the deep adjacent ocean, respectively. The continental slope is quite steep, the parameter $r = \Delta h/2h = (h_i - h_{i-1})/(h_i + h_{i-1})$ defined by Beckmann and Haidvogel [3] having a maximum value of 0.423 at a distance about 20 km from the coastline. This parameter is used to measure the hydrostatic consistency associated with the σ-coordinate system by Haney [15]. The grid size is enhanced on the continental shelf and slope in order to improve resolution in these regions. The values of parameters used in these simulations are shown in Table Ic.

With an equatorward wind, which is commonly observed during spring and summer in this region, i.e., with

$$\tau^{\xi} = 0, \quad \tau^{\eta} = 1 \times 10^{-4} \times (0.1 - 0.5\cos(2\pi t/\text{month})),$$

it is known that the equatorward wind drives the offshore transport of surface water in the surface Ekman layer and causes upwelling near the coastal boundary which leads to a lowering of sea-level at the coast. We have run the model for 105 days to demonstrate the phenomenology. Contours of the surface elevation in Fig. 9a show the expected slope towards the coast. Figure 9b shows the barotropic velocity field. The velocity field shows a meandering equatorward jet with dipole eddies. The eddies in the offshore side of the jet ate anticyclonic and eddies in another side are cyclonic. Cross-channel sections of meridional current plotted in Fig. 10a clearly shows the upper layer equatorward coastal jet and a deep poleward return flow. Both features are reminiscent of the observed currents in this region. The cross section of density in Fig. 10b shows that the isopycnals slope upward towards the shore as cooler, denser water wells up to replace warmer, less dense surface waters. Time steps used in this experiment are 216 s (400 steps per day) for the internal mode and 10.8 s for the external mode. It takes about 48 h on IBM RS/6000 (model 560) for the 120-day

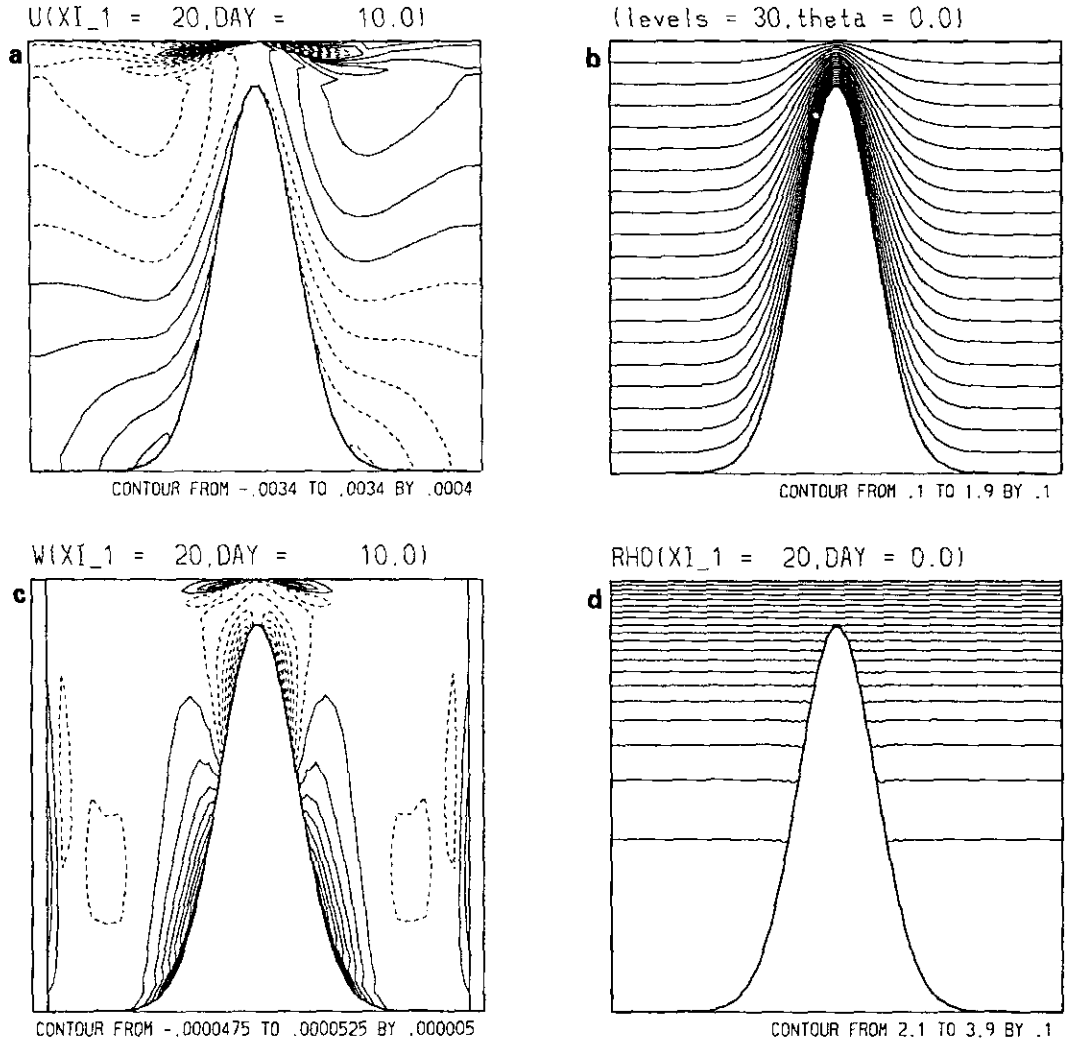

FIG. 5. Same as Fig. 4 but in σ-coordinate.

simulation. More detail simulations of the California current system are reported in Song and Haidvogel [27].

6. CONCLUSION

In this paper, we have introduced a new general vertical coordinate (s-coordinate) system to model stratified flow in the coastal ocean. The model equations are the three-dimensional, free surface, primitive equations with orthogonal curvilinear horizontal coordinates following the irregular coastal boundaries. Several numerical modeling techniques have been successfully tested. The implicit finite element formulation in the vertical has the advantages of achieving higher accuracy of solution and allowing larger time steps. The higher-order Lagrange quadrature technique is essential to calculate the dynamic pressure and vertical velocity accurately since both variables are very sensitive to numerical noise. Finally, surface layer mixing is naturally applied in the s-coordinate which allows a uniformly high resolution in the upper ocean.

Three realistic problems have been used to verify the capabilities of the model. The diurnal cycling problem represents a physical process of ocean surface responding to strong atmospheric forcing. The model has proven itself to be capable of handling surface mixing dynamics. A tall seamount bathymetry provides a severe bottom topography which may lead to numerical errors and instabilities. The model has proven to be stable and accurate even for a strong stratification. Moreover, over the seamount bathymetry, turbulent closure mixing has been applied to a wind-driven flow and generated the expected surface mixed layer. The last realistic test problem is the simulation of the California current system, which is widely recognized as a complex coastal ocean problem. The model has been shown to be capable of dealing

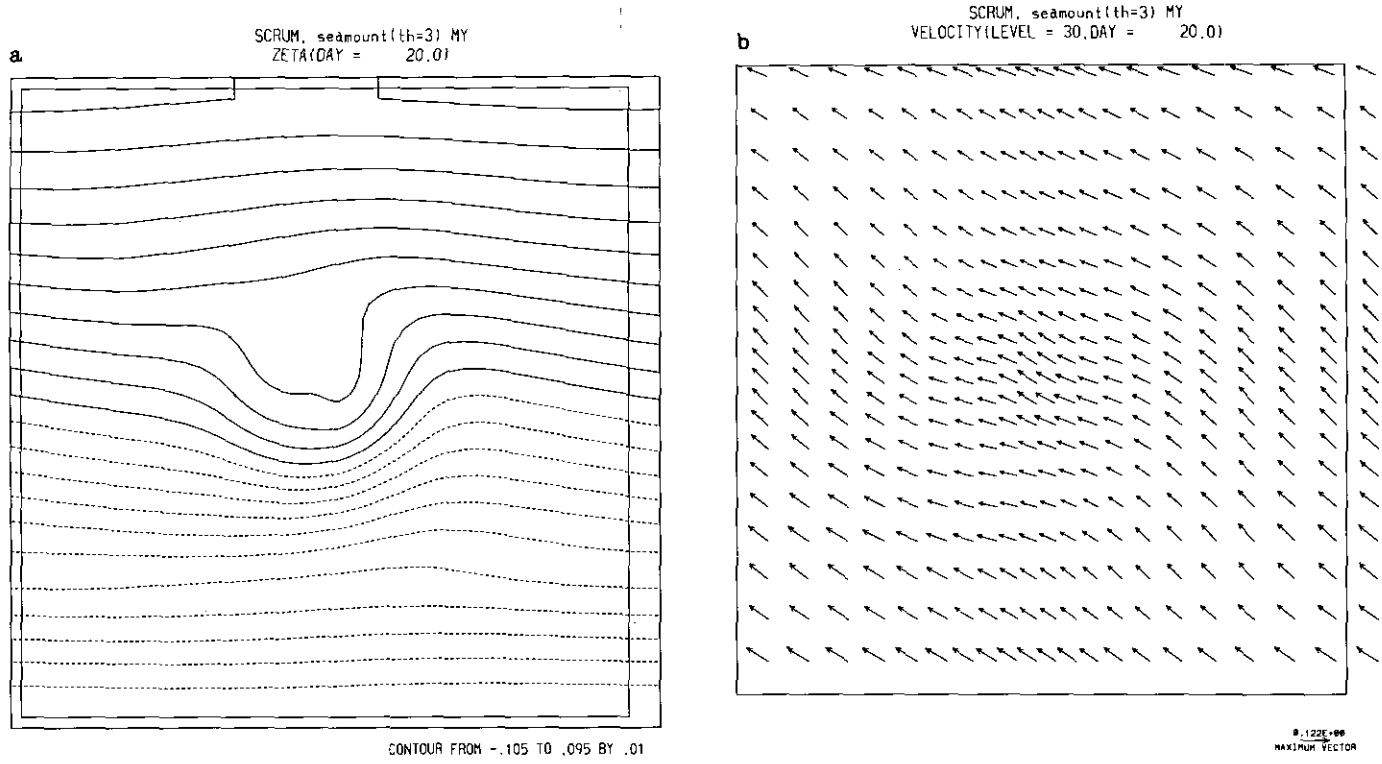

FIG. 6. (a) Contours of surface elevation; (b) the surface velocity field driven by a constant east wind on the seamount bathymetry.

with the irregular coastal geometry, continental shelf slope topography, and applied wind forcing.

The model formulated in this paper is designed to be a useful tool for studying complex coastal ocean problems as well as the basin-scale ocean circulation. Based on the model formulation, a general software package—SCRUM, standing for S-coordinate Rutgers University model—has been developed and tested for different problems. The three examples presented in Section 5 illustrate the results generated from the model package. Further applications of the model to real oceanographic problem are the subject of ongoing research.

APPENDIX A: FINITE ELEMENT APPROXIMATION

In this appendix, we describe the Galerkin finite element method used to solve Eqs. (3.11)–(3.13) for $\tilde{U}$. First we replace the differential equations and boundary conditions by the variational identity

$$\frac{1}{\lambda\Delta t}\int_{-1}^{0} H_\theta \tilde{U} V\, ds + \int_{-1}^{0}\left(-H_\theta \Omega \tilde{U} + \frac{K}{H_\theta}\frac{\partial \tilde{U}}{\partial s}\right)\frac{\partial V}{\partial s}\, ds = \int_{-1}^{0} \tilde{R}_c(s) V(s)\, ds + V(0)\tilde{\tau}_s - V(-1)\tilde{\tau}_b \tag{A.1}$$

where $\tilde{R}_c$ is the right-hand side of Eq. (3.13) and $V(s)$ is an arbitrary differential function. Within the class of H_0^1 functions [11], the variational identity (A.1) is equivalent to the boundary problem (3.10)–(3.13). Using the Galerkin finite element discretization, some conservation properties can be preserved automatically. In addition, the surface and bottom boundary conditions can be naturally applied to the right-hand side of the variational equations.

The basis function can be written as

$$\gamma_k(s) = \begin{cases} (s - s_{k-1})/\Delta s, & s \in [s_{k-1}, s_k], \\ (s_{k+1} - s)/\Delta s, & s \in [s_k, s_{k+1}], \\ 0, & \text{otherwise}, \end{cases}$$

where the domain $[-1, 0]$ is divided into N equal subdomains (elements) and $\Delta s = s_{k+1} - s_k$. Expanding $\tilde{U}$ and $V(s)$ by basis functions $\gamma_k(s)$ and evaluating the integrals, we obtain identity (A.1) in the form [18]

$$\begin{aligned} &\frac{1}{\lambda\Delta t}\sum_{k=0}^{k=N-1}\Delta z_k\{(\tilde{U}_k V_k + \tilde{U}_{k+1}V_{k+1})/3 + (\tilde{U}_{k+1}V_k + \tilde{U}_k V_{k+1})/6\} \\ &- \sum_{k=0}^{k=N-1}(2\omega_k\tilde{U}_k + \omega_{k+1}\tilde{U}_k + \omega_k\tilde{U}_{k+1} + 2\omega_{k+1}\tilde{U}_{k+1})(V_{k+1} - V_k)/6 \\ &+ \sum_{k=0}^{k=N-1}(\tilde{U}_{k+1} - \tilde{U}_k)K_{k+1/2}(V_{k+1} - V_k)/\Delta z_k \\ &= \sum_{k=0}^{k=N-1}\Delta s(2\tilde{R}_{c,k}V_k + \tilde{R}_{c,k+1}V_k + \tilde{R}_{c,k}V_{k+1} + 2\tilde{R}_{c,k+1}V_{k+1})/6 \\ &+ \tilde{\tau}_s V_N - \tilde{\tau}_b V_0, \end{aligned} \tag{A.2}$$

where $\Delta z_k = H_\theta \Delta s_k$ is the vertical grid spacing in the physical

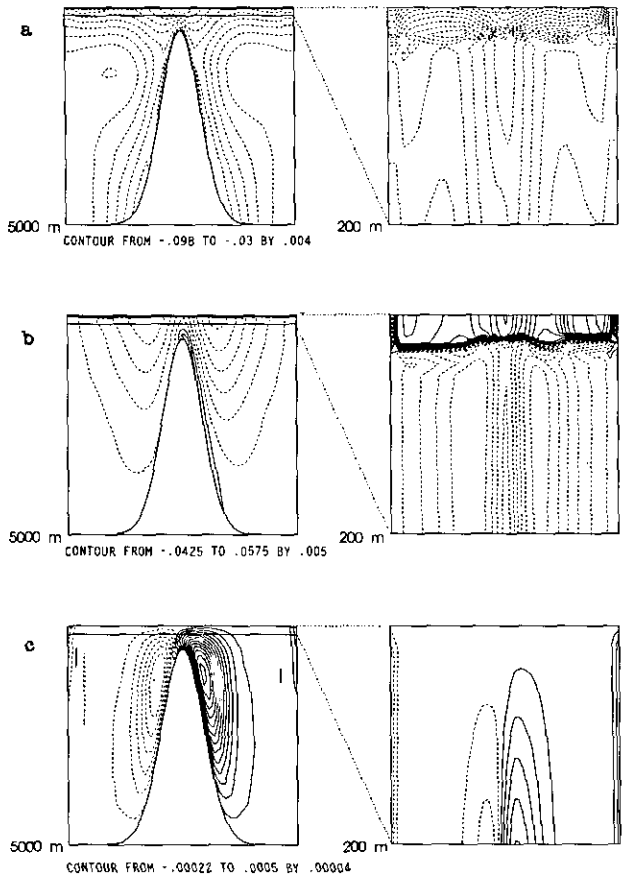

FIG. 7. Conours of cross sections through the center of the seamount: (a) for u; (b) for v; (c) for w with Mellor–Yamada level-2 turbulent mixing after 20 days driven by a constant east wind.

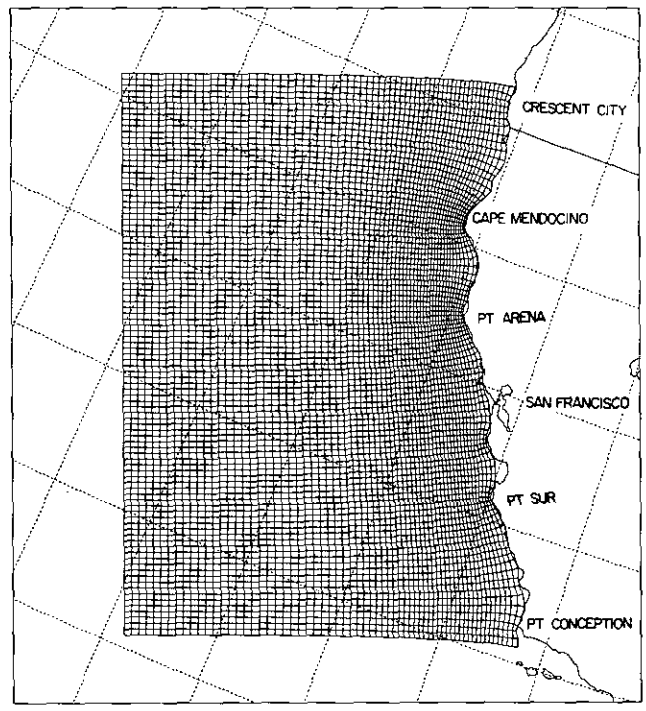

FIG. 8. Grid cell configuration for California coast.

domain and $\omega = H_\theta \Omega$. This variational equation is required to hold for all $\{V_k\}$. Setting the coefficient of V_k equal to zero, we recover the tridiagonal system,

$$-A_k \tilde{U}_{k-1} + B_k \tilde{U}_k - C_k \tilde{U}_{k+1} = D_k, \quad k = 0, ..., N. \quad \text{(A.3)}$$

The coefficients A_k, B_k, C_k, and D_k are the analogous of Lardner and Song [18]. The tridiagonal system can be straightforwardly solved in $O(N)$ operations [10] by forward elimination,

$$B_k = B_k - A_k C_{k-1}/B_{k-1}, \quad D_k = D_k + A_k D_{k-1}/B_{k-1}, \quad k = 1, ..., N, \quad \text{(A.4)}$$

and back substitution,

$$\tilde{U}_N = D_N/B_N, \quad \tilde{U}_k = (D_k + C_k \tilde{U}_{k+1})/B_k, \quad k = N-1, ..., 0. \quad \text{(A.5)}$$

From Eq. (A.3), velocity profiles $\tilde{U}^{n+1}$ can therefore be obtained, and similar procedures yield temperature and salinity profiles. As shown by Lardner and Song [18] the above forward elimination and back substitution can relax the CFI restriction due to vertical discretization; stability is guaranteed so long as

$$|\omega_k| < \min\left\{\frac{\Delta z}{2\lambda\,\Delta t}, \frac{\Delta z}{6\lambda\,\Delta t} + \frac{6K}{5\,\Delta z}\right\}. \quad \text{(A.6)}$$

APPENDIX B: AN ADVECTION AND DIFFUSION PROBLEM

In this appendix, we shall show how the above finite element technique works for a simple one-dimensional advection–diffusion problem like (3.10)–(3.11). The problem considered here is

$$\frac{\partial S}{\partial t} + w\frac{\partial S}{\partial z} - \frac{\partial}{\partial z}\left(K\frac{\partial S}{\partial z}\right) = 0 \quad \text{(B.1)}$$

with

$$K\frac{\partial S}{\partial z} = \tau_s, \quad \text{at } z = \zeta; \quad \text{(B.2)}$$

TABLE Ic

Values of the Parameters Used in the California Current Simulations

Symbol	Value	Definition
L	98	Number of points in η direction
M	65	Number of points in ξ direction
N	30	Vertical levels
h_c	100 m	Parameter in s-coordinate
θ	3	Parameter in s-coordinate
$h_{\min}$	86 m	Minimum of water depth
$h_{\max}$	4600 m	Maximum of water depth
$\bar{\rho}$	$4. - 3.2 \times e^{z/200}$	Background density stratification
A_{MH}	$3 \times 10^3 m^2 s^{-1}$	Harmonic viscosity coefficient
A_{HH}	$1 \times 10^3 m^2 s^{-1}$	Harmonic diffusion coefficient
K_M	$1 \times 10^{-3} + 2 \times 10^{-4} \times e^{z/200}$	Vertical viscosity coefficient
K_H	$1 \times 10^{-4} + 2 \times 10^{-4} \times e^{z/200}$	Vertical diffusivity coefficient

$$K\frac{\partial S}{\partial z} = \tau_b, \quad \text{at } z = -h. \tag{B.3}$$

This problem has the exact solution

$$S(z, t) = \frac{c}{\sqrt{4\pi Kt}} \exp(-(z - z_0 - wt)^2/4Kt), \tag{B.4}$$

providing the initial condition is a point source $S(z, 0) = c\,\delta(z_0)$, which is discretized as

$$S(z_k, 0) = \begin{cases} c/\Delta z_k, & \text{if } k = k_0, \\ 0, & \text{otherwise.} \end{cases}$$

This initial condition is discontinuous and chosen to test how severe a problem the algorithm can handle. The corresponding boundary conditions are

$$\tau_s = S(\zeta, t)\frac{-\zeta + z_0 + wt}{2t}, \quad \tau_b = S(-h, t)\frac{h + z_0 + wt}{2t}. \tag{B.5}$$

The nondimensional parameters used are $K = 0.001$, $c = 2000$, $w = -0.00001$, and depth $h = 1000$ m in this problem. The depth is divided into 30 levels with about 20 levels in the upper 200 m, corresponding to $h_c = 50$ m and $\theta = 3.2$ in the s-coordinate, and to a minimum grid size of about 2.4 m near the surface. Based on this grid spacing, the CFL condition is $\Delta z^2/(2K) \approx 3000$ s. Table II gives the computed solutions after 200 time steps (about 42 days) using a time step of 18,000 s (5 h), six times longer than that allowed by the CFL condition. For simplicity, only the values at even levels are presented here. The errors listed are relative errors when the solution is greater than 0.05 or else absolute errors between the exact solution (B.4) and the computed solution. From this test problem, we can see that the finite element method can achieve a highly accurate solution even for a discontinuous initial source.

APPENDIX C: CALCULATION OF THE PRESSURE AND Ω PROFILES

In this appendix, we describe a quadrature integration technique used for calculating the pressure and Ω profiles. In the s-coordinate system, the dynamic pressure can be obtained by integrating the density from the surface

$$\phi = \frac{g}{\rho_0}\int_s^0 H_\theta(\rho_0 + \bar{\rho})\,ds + \frac{g}{\rho_0}\int_s^0 H_\theta(\rho - \bar{\rho})\,ds, \tag{C.1}$$

where $\bar{\rho}$, the background profile of the perturbation density ρ, is chosen such that the first integral can be evaluated analytically and $\rho - \bar{\rho}$ in the second term can be minimized. For example, by choosing $\bar{\rho} = \bar{\rho}_1(z) + \bar{\rho}_2(x, y)$, where $\bar{\rho}_1(z)$ is the mean stratification and $\bar{\rho}_2(x, y)$ is the surface values of $\rho - \bar{\rho}_1$, the first integral can be calculated analytically and the second integrand has zero value at the surface such that it can be calculated accurately.

In order to obtain Ω and avoid calculating ζ from Eq. (2.26), we subtract Eq. (2.26) from (3.3) and have

$$\frac{\partial}{\partial s}\left(\frac{H_\theta \Omega}{mn}\right) = -\frac{\partial}{\partial \xi}\left(\frac{H_\theta u - D\bar{u}}{n}\right) - \frac{\partial}{\partial \eta}\left(\frac{H_\theta v - D\bar{v}}{m}\right).$$

Then

$$H_\theta \Omega = mn\int_s^0 \left\{\frac{\partial}{\partial \xi}\left(\frac{H_\theta u - D\bar{u}}{n}\right) + \frac{\partial}{\partial \eta}\left(\frac{H_\theta v - D\bar{v}}{m}\right)\right\} ds. \tag{C.2}$$

By using a traditional integrating method to calculate (C.1) and (C.2), it is difficult to achieve a high accuracy for the uppermost levels since other levels outside of the integral domain are not used. However, by using the Lagrange quadrature technique as shown by Leslie and Purser [19], higher order accuracy can be achieved. The basic idea is to interpolate the integrand by Lagrange polynomials and then use the quadrature formula to calculate the integral.

Let $\psi(s_i)$ be a generic integrand at level s_i, then, the $2m$th-order Lagrange interpolation of $\{\psi(s_i)\}$ in the domain of $[-1,1]$ can be written

$$\psi(s) \approx \sum_{i=J_1}^{i=J_2} I_i(s)\psi(s_i), \quad I_i(s) = \prod_{j\neq i, j\in[J_1, J_2]} \frac{s - s_j}{s_i - s_j}, \tag{C.3}$$

where $s \in [s_k, s_{k+1}]$, $J_1 = \max(0, k - m)$, and $J_2 = \min(N, k + m)$.Then, the integrals of (C.1) and (C.2) have the form

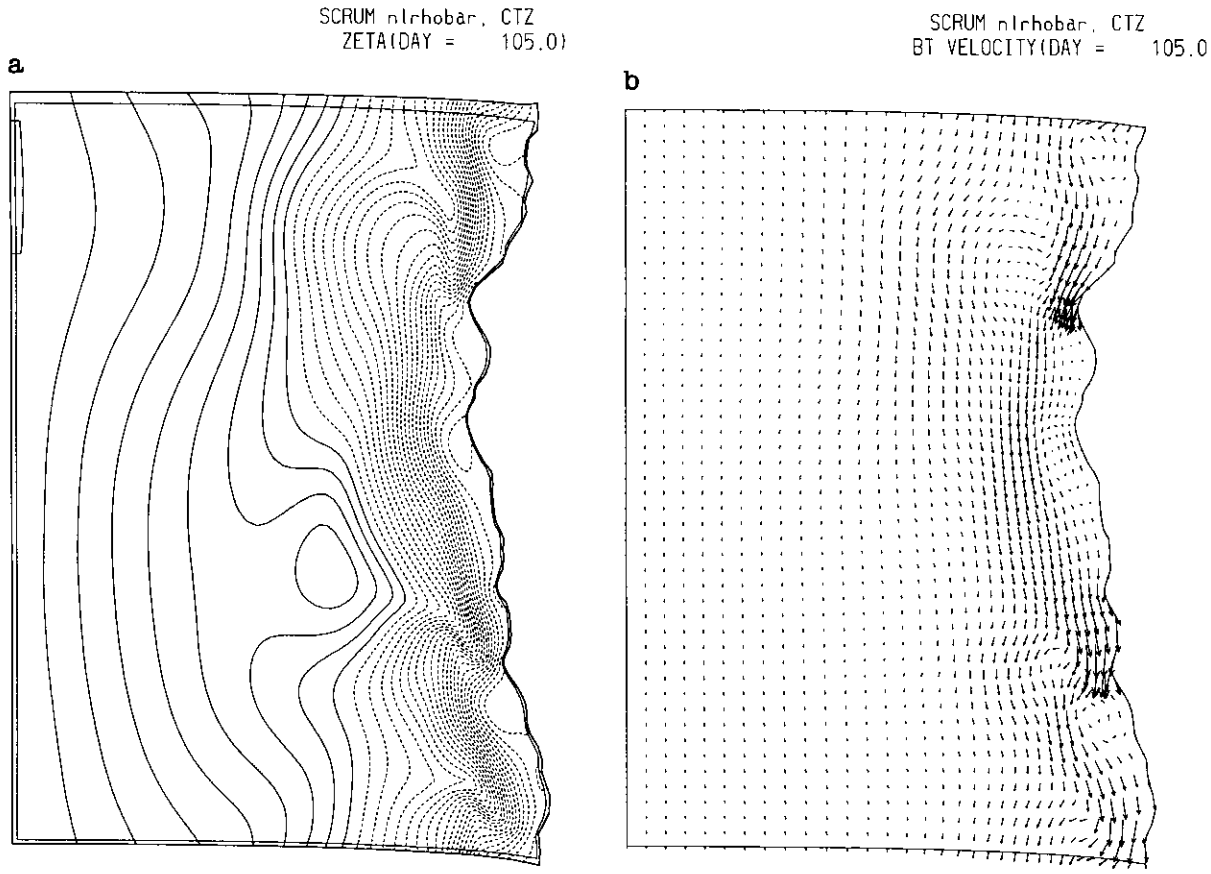

FIG. 9. (a) contour of surface elevation; (b) surface velocity field after 105 days forced by a time variable wind.

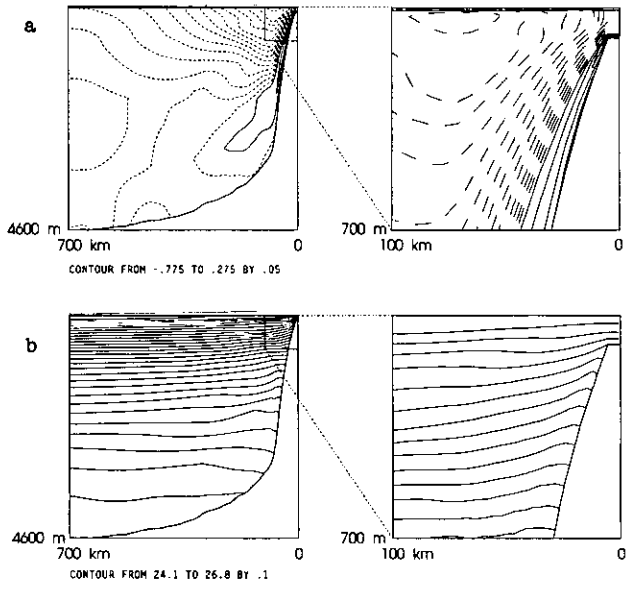

FIG. 10. Results after 105 days forced by a time variable wind: (a) section of u across-shelf near Pt. Arena, u, is the along-coast component, dashed contour lines for equatorward flow; (b) section of density across-shelf near Pt. Arena.

TABLE II

Computed Solution and Exact Solution of a 1D Advection and Diffusion Problem after 200 Time Steps (42 Days)

Level	Depth (m)	Exact	Computed	Error
30	0.00	7.8248	7.8294	−0.0006
28	4.72	8.0795	8.0841	−0.0006
26	9.69	8.3291	8.3338	−0.0006
24	15.23	8.5812	8.5860	−0.0006
22	21.74	8.8390	8.8441	−0.0006
20	29.80	9.0949	9.1003	−0.0006
18	40.29	9.3126	9.3187	−0.0007
16	54.53	9.3847	9.3920	−0.0008
14	74.54	9.0472	9.0564	−0.0010
12	103.40	7.7829	7.7952	−0.0016
10	145.83	5.0589	5.0692	−0.0020
8	209.04	1.6764	1.6470	0.0178
6	304.12	0.1122	0.0642	0.0480
4	448.02	0.0002	0.0003	−0.0001
2	666.71	0.0000	0.0000	0.0000
0	1000.00	0.0000	0.0000	0.0000

Note. Errors listed are relative errors when the values of the exact solution are greater than 0.05.

TABLE IIIa

Numerical Integration Errors for Function $\psi = \sin(\pi s)$ by the Trapezoidal, Simpson, and Quadrature Methods, Respectively

$\psi = \sin(\pi s)$		Error		
Level	Exact	Trapezoidal	Simpson	Quadrature
16	0.074470	−0.7577E-03	0.6318E-05	0.2012E-06
14	0.263036	−0.2676E-02	0.2220E-04	0.6855E-06
12	0.477465	−0.4858E-02	0.4029E-04	0.7153E-06
10	0.617423	−0.6282E-02	0.5203E-04	0.7749E-06
8	0.617423	−0.6282E-02	0.5203E-04	0.7749E-06
6	0.477465	−0.4858E-02	0.4023E-04	0.8047E-06
4	0.263036	−0.2676E-02	0.2220E-04	0.2682E-06
2	0.074470	−0.7577E-03	0.6340E-05	−0.2384E-06
0	0.000000	0.1863E-08	0.1766E-07	−0.4042E-06

TABLE IIIb

Numerical Integration Errors for Function $\psi = 1/(1.5 - s)^2$ by the Trapezoidal, Simpson, and Quadrature Methods, Respectively

$\psi = 1/(1.5 - s)^2$		Error		
Level	Exact	Trapezoidal	Simpson	Quadrature
16	0.615385	0.1087E-01	0.4640E-03	0.6318E-05
14	0.941176	0.1387E-01	0.5340E-03	0.7272E-05
12	1.142857	0.1501E-01	0.5507E-03	0.7391E-05
10	1.280000	0.1554E-01	0.5561E-03	0.7391E-05
8	1.379310	0.1581E-01	0.5581E-03	0.7391E-05
6	1.454545	0.1597E-01	0.5589E-03	0.7391E-05
4	1.513514	0.1607E-01	0.5594E-03	0.7510E-05
2	1.560976	0.1613E-01	0.5597E-03	0.7749E-05
0	1.600000	0.1617E-01	0.5598E-03	0.7629E-05

$$\int_{s_k}^{1} \psi(s)\, ds \approx \sum_{i=J_1}^{i=J_2} \int_{s_k}^{1} I_i(s)\, ds\, \psi(s_i) = \sum_{i=J_1}^{i=J_2} c_{k,i}\, \psi_i. \qquad \text{(C.4)}$$

From integral approximation theory, we know that the above quadrature formula can achieve $(2m + 1)$th-order accuracy. In order to verify this technique, several numerical tests have been carried out to compare it with the traditional trapezoidal formula and Simpson's formula. The comparison is given in Table IIIa for the integrand function $\psi(s) = \sin(\pi s)$ and in Table IIIb for the integrand function $\psi(s) = 1/(1.5 - s)^2$. For simplicity, only the values at even levels are presented here. Both integrals are calculated from a level s to 1 in $[-1, 1]$ with 16 equally spaced levels with $m = 2$ and 4 in the Lagrange interpolation, respectively. From these examples we can see that the accuracy can be significantly improved by using the quadrature formulation.

ACKNOWLEDGMENTS

The authors thank J. Price for providing his 1D mixed layer code and for suggesting comments on the diurnal test problem. John Wilkin, Anne-Marie Treguier, John McCalpin, and Greg Holloway have carefully read through the manuscript and many suggestions from them are appreciated. Our special thanks go to K. Hedström for her constant help in forming the SCRUM package. Appreciation is also due to Laurel Henderson for the drawing of some figures. This work was funded by the Office of Naval Research under Grant No. N00014-91-J1557.

REFERENCES

1. S. G. Alderson, *Dyn. Atmos. Oceans* **15,** 59 (1990).
2. A. Arakawa and V. R. Lamb, in *Methods in Computational Physics, Vol. 17 (Academic Press, New York/London, 1977), p. 173.*
3. A. Beckmann and D. Haidvogel, *J. Phys. Oceanogr.* **23** (8), 1736 (1993).
4. K. H. Brink, *Coastal Ocean Processes* (Woods Hole Oceanographic Institute, Woods Hole, MA 02543, 1992).
5. D. Chapman and D. Haidvogel, *Geophys. Astrophys. Fluid Dyn.* **64,** 31 (1992).
6. A. Davies (Ed.) *Modeling Marine Systems, I, II* (CRC Press, Boca Raton, FL, 1990).
7. D. R. Durran, *Mon. Weather Rev.* **119,** 702 (1991).
8. B. Galperin, L. H. Kantha, S. Hassid, and A. Rosati, *J. Atmos. Sci.* **45,** 55 (1988).
9. A. E. Gill, *Atmosphere–Ocean Dynamics* (Academic Press, Orlando, FL, 1982).
10. G. H. Golub and C. F. van Loan, *Matrix Computations* (Johns Hopkins Univ. Press, Baltimore, 1983).
11. M. D. Gunzburger, *Finite Element Methods for Viscous Incompressible Flows* (Academic Press, San Diego, 1989).
12. D. Haidvogel, J. Wilkin, and R. Young, *J. Comput. Phys.* **94,** 151 (1991).
13. D. Haidvogel, A. Beckmann, and K. Hedström, *J. Geophys. Res.* **96,** 15017 (1991).
14. B. Henderson-Sellers and A. M. Davies, in *Annual Review of Num. Fluid Mechanics and Heat Transfer,* Vol. 2 (Academic Press, New York/London, 1989), p. 86.
15. R. L. Haney, *J. Phys. Oceanogr.* **21,** 610 (1991).
16. A. Kasahara, *Mon. Weather Rev.* **102,** 509 (1974).
17. R. W. Lardner and P. Smoczynski, *Proc. R. Soc. London Ser. A* **430,** 263 (1990).
18. R. W. Lardner and Y. Song, *Int. J. Numer. Methods Eng.* **32,** 1303 (1991).
19. L. M. Leslie and R. J. Purser, *Mon. Weather Rev.* **119,** 1612 (1991).
20. J. D. McCalpin, Ph.D. thesis, Florida State University, Tallahassee, 1990 (unpublished).
21. G. L. Mellor and T. Yamada, *Rev. Geophys. Space Phys.* **20,** 851 (1982).
22. N. A. Phillips, *J. Meteorol.* **14,** 184 (1957).
23. J. F. Price N. K. Mooers, and J. C. Van Leer, *J. Phys. Oceanogr.* **8,** 582 (1978).
24. J. F. Price, R. A. Weller, and R. Pinkel, *J. Geophys. Res.* **91,** 8411 (1986).
25. M. M. Rienecker, C. N. K. Mooers, and A. R. Robinson, *J. Phys. Oceanogr.* **8,** 1189 (1987).
26. Y. Song and T. Tang, *Mon. Weather Rev.* **122** (1), 223 (1994).
27. Y. Song and D. Haidvogel, in *Estuarine and Coastal Modeling, ings, 3rd Int. Conf., ASCE, Chicago, 1993,* edited by M. L. Spaulding et al., p. 216.
28. G. Veronis, in *Numerical Models of Ocean Circulations, Washington, DC, 1975,* p. 133.
29. J. Wilkin and K. Hedström, unpublished manuscript, 1991.